Atlas-guided Automated Analysis of Small-Animal PET Studies

Daniel Gutierrez, *Member, IEEE*, and Habib Zaidi, *Senior Member, IEEE*

***Abstract*–This work aims to develop a methodology for automated atlas-guided analysis of small animal PET data through deformable registration to an anthropomorphic mouse atlas. A non-rigid registration technique is used to put into correspondence relevant anatomic regions of rodents to the predefined atlas. The technique consists in registering CT images from actual mouse PET/CT data to corresponding CT images of the Digimouse atlas, thus providing a pre-segmented anatomical model consisting of 21 anatomical regions suitable for automated analysis. Image registration is performed using the Elastix package, which is a modular toolbox based on the ITK library allowing the implementation of various image registration algorithms. Once the optimal parameters were derived, these were applied to all data sets. The accuracy of image registration was assessed by segmenting mice CT images into 7 regions: brain, lungs, heart, kidneys, bladder, skeleton and rest of the body. This was realized previous to image registration in a semi-automated way using the ITK-Snap toolbox. Each segmented mouse was transformed using the output transformation parameters obtained during CT image registration. The resulting segmentation was compared with the original Digimouse atlas to quantify image registration accuracy using established figures of merit such as Dice coefficient and Hausdorff distance showing fair to excellent agreement and a mean registration mismatch distance of about 6 mm. Pre-registration was applied to some PET images which were slightly misaligned with the corresponding CT images. PET images were then transformed using the same method used earlier. The results demonstrate good quantification accuracy in most regions, especially the brain. As expected, relatively large deviations were obtained for the bladder. It can be concluded that the proposed automated technique is reliable and suitable for fast quantification of preclinical PET data in large serial studies.**

***Index Terms* — PET/CT, quantification, deformable registration, atlas, mouse.**

I. INTRODUCTION

One of the important advantages of PET is its ability to generate quantitative dynamic images of regional tracer uptake, resulting in regional measurements of tracer kinetics that can be correlated to clinical variables such as response to therapy or tumor progression. In this way, quantitative disease physiology can be related to disease behavior in various applications including preclinical therapy trials. For example, the quantitative analysis of tracer uptake enables a better management of therapy for an individual animal model and eventually assess the overall response of a therapy in a population of transgenic animals [1].

The automated quantitative assessment of PET data is attractive and will revolutionize the practice of molecular imaging since it can lower variability across institutions and may enhance the consistency of image interpretation independent of reader experience. For example, the development of tracer-specific small animal PET probabilistic atlases [2] correlated with anatomical templates enabled automated Volume-of-Interest (VoI) or voxel-based analysis of small animal PET data with minimal user interaction [3]. One such software tool was developed by Kesner *et al.* [4] to enable the assessment of the biodistribution of PET tracers using small animal PET data. This was achieved though non-rigid registration of a digital mouse atlas with the animal PET image followed by automated calculation of tracer concentrations in 22 predefined VoIs located at major organs. The development of advanced anatomical models including both stylized and more realistic voxel-based mouse [5-7] and rat [8, 9] models obtained from serial cryosections or dedicated high resolution small animal CT and MRI scanners will certainly help to support ongoing research in this area [10].

Our objective in this work is to develop and assess the performance of Atlas-guided automated analysis of PET data based on anthropomorphic models depicting the anatomy and physiological functions of rodents combined with retrospective registration-guided methods for motion artifact reduction thus enabling correct localization and accurate quantification of molecular targets. Our approach is different from the one adopted by Kesner *et al* [4] in the sense that we are aiming to develop a fully automated analysis procedure which does not require user interaction and do not rely on fiducially markers or internal landmarks.

A substantial number of techniques have been proposed to achieve the goal of multimodal medical image registration [11, 12]. Image registration techniques permit the alignment of multimodality images through one of the two main categories of methods: rigid-body transformation thus ignoring organ deformation owing to, for example, respiratory motion; and non-rigid registration algorithms that can compensate for perceived organ deformation for different imaging modalities, or align images from different subjects [13]. However, despite progress made during the last few years, many image registration problems particularly for small animal imaging

This work was supported by the Swiss National Foundation under grant No. 31003A-125246.

Daniel Gutierrez is with Division of Nuclear Medicine and Molecular Imaging, Geneva University Hospital, CH-1211 Geneva, Switzerland (e-mail: Daniel.GutierrezRios@unige.ch)

Habib Zaidi is with the Division of Nuclear Medicine and Molecular Imaging, Geneva University Hospital, CH-1211 Geneva, Switzerland, Geneva Neuroscience Center, Geneva University, Geneva, Switzerland, and Department of Nuclear Medicine and Molecular Imaging, University Medical Center Gronigen, University of Groningen, Groningen, Netherlands (e-mail: habib.zaidi@hcuge.ch).

remain unsolved, and as such this area is likely going to continue to be an active field of research in the future [14].

The rationale of the automated 3D registration procedure used in this work is to transform PET images of the actual animal with the transformation parameters obtained during the image registration between the corresponding actual CT images and CT images of the Digimouse dataset consisting of cryogenic, PET and segmented images [6]. Registration and transformation procedures were performed using the Elastix and Transformix software tools [15], respectively.

3D image registration performance was assessed using the Dice coefficient (D_{coeff}) and the Hausdorff Distance (*HD*) which are standard image registration/segmentation metrics [5, 6]. The accuracy of automated PET data analysis was qualified through comparison with non-transformed measures using a method similar to the one used by Kesner *et al* [4].

II. Materials and Methods

A. Mouse Atlas

We have selected the Digimouse dataset [6] as a reference 3D atlas because it is composed of a 3D Atlas of preregistered PET, CT and cryosection slices. A representative slice of this model is shown in Figure 1. Processed images are available in 8-bit coding mode (256 gray levels) that could lead to loose of information during the registration process. For this reason, we have re-processed raw images (available in 32-bits floating-point) to obtain typical 16-bit CT images and 32-bit PET images.

B. Laboratory mice data

The sample of laboratory animals included in this work is composed of 8 mice PET/CT datasets completed with segmentations performed in our lab:

a) One mouse acquired on the FLEX Triumph™ preclinical PET/CT scanner (Gamma Medica-Ideas, Nortridge, CA) [16], consisting of 16-bit CT images of 256×256×512 voxels of 0.17×0.17×0.17 mm^3, and 32-bit PET images of 256×256×256 voxels of 0.4×0.4×0.4mm^3.

b) 4 mice datasets acquired on the Siemens MicroFocus scanner kindly provided by the Crump institute at UCLA composed of CT images of 256×256×496 pixels of 0.2×0.2×0.2mm^3 coded on 16-bits and PET images of 128×128×95 pixels of 0.4×0.4×0.8mm^3 coded on 32-bits.

c) 3 mice datasets from the Applied Sciences laboratory at Uppsala, acquired on the Triumph™ scanner (GE Healthcare), consisting of CT images of 240×240×63 pixels of 0.25×0.25×1.175mm^3 coded on 16-bits and PET images of 240×240×63 pixels of 0.25×0.25×1.175 mm^3 coded on 16 bits.

Most of these mice had tumor xenografts with heavy morphological deformations that increased the difficulty of the image registration task.

C. Simulated mice images

To perform additional analysis under controlled conditions and obtain more relevant statistical analysis, we have completed our sample with 17 simulated PET/CT datasets.

First we created voxelized phantoms produced using the MOBY digital mouse phantom software [5] taking into account variations in mouse size that were determined randomly using a normal distribution as described by Kesner et al. [4].

The output of the software represents an average acquisition of 120 seconds resulting in two voxelized phantoms with a voxel size of 0.2×0.2×0.468 mm^3:

- An activity map, where the activity concentration in the individual organs is obtained by randomly choosing the activity concentration value for each organ based on normal distribution reported by Kesner et al. [4].
- An attenuation map at the energy of the radionuclide defined in the parameters file, in our case FDG-PET (511 keV).

The same software was used to produce segmented images in a semi-automated way using the input parameter file by putting activity only in one organ at a time. Finally we combined the images produced by all the considered organs to produce the segmented image. The final image was manually corrected to fill holes in the heart and lung regions to obtain images similar to those of the Digimouse atlas. An example is shown in Fig. 2.

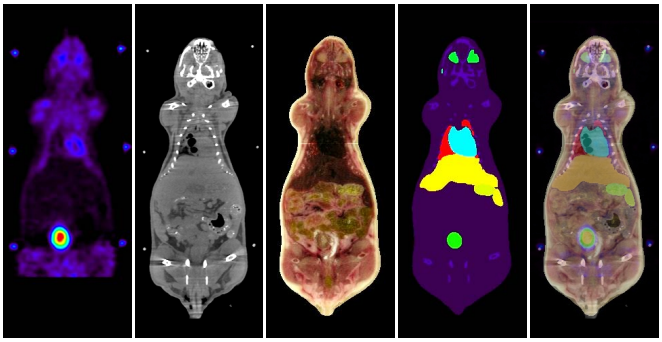

Fig. 1. Spatially registered images for a coronal slice through the Digimouse model.

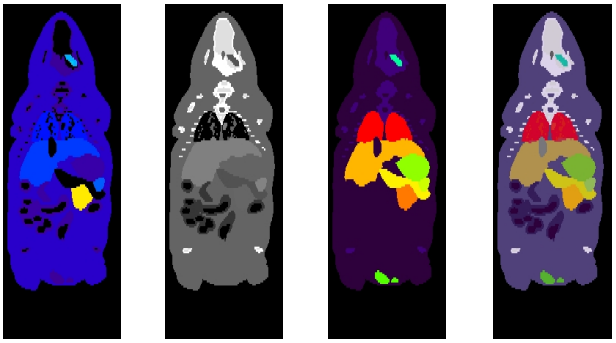

Fig. 2. Example of a voxelized model generated using the MOBY software.

The x-ray CT projector of the MOBY software suite [17] was used to produce 360 projection images with characteristics similar to the FLEX Triumph™ microCT:

- Object to source distance = 22.2 cm
- Object to detector distance = 6.8 cm
- Half fan angle = 19°
- Pixel size of 0.2×02 mm^2.

These projections were reconstructed to obtain CT images with a voxel size of 0.2×0.2×0.4 mm^3 using Feldkamp's algorithm [18] available as part of the Matlab image reconstruction toolbox developed by Dr Fessler[1].

Image reconstruction, including attenuation correction, was performed from the voxelized phantoms (attenuation and activity) processed using the STIR (Software for Tomographic Image Reconstruction) package [19] using 3D OSEM algorithm with inter-update Metz filtering [20]. Examples of X-ray projection images, CT and PET reconstructions are shown in Fig. 3.

D. Deformable image registration

As stated earlier, we register the actual mouse (moving image) to the Digimouse atlas (fixed image) without the use of fiducial markers.

The *elastix* image registration package was used in this work [15]. It consists on a collection of algorithms developed based on the Insight Toolkit (ITK) libraries. This package also contains the *transformix* program that uses the transformation parameters output file obtained during the registration made with *elastix*.

This software was conceived as a modular image registration tool (Fig. 4). Each of these modules can be parameterized individually depending on the needs of each particular situation.

First of all, we verify that PET/CT images are correctly pre-registered; then we proceed with CT to CT image registration between the actual mouse and Digimouse atlas. Many theoretical considerations and practical tests were conducted to find the optimal parameters used in this work. Image registration was performed between 3D CT images of the actual mouse and corresponding images of the Digimouse atlas in three steps:

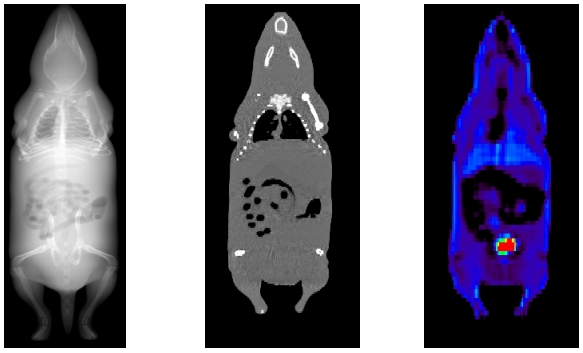

X-ray Projection **CT reconstruction** **PET reconstruction**

Fig. 3. X-ray projection image and PET/CT reconstructed images obtained from the MOBY phantom.

[1] http://www.eecs.umich.edu/~fessler/

1. *Affine registration:* this was realized to pre-align both CT images and facilitate the task of non-rigid registration.
2. *B-Spline non-rigid registration:* this is performed to achieve a good alignment in size and shape of both 3D images. Most of the time, this step does not register accurately mice internal organs but it is very effective for full mice shape.
3. *Masked B-Spline non-rigid registration:* This step is performed to obtain a finer registration of internal organs by avoiding spending computer resources on the part located outside of the mice. We have used one unique mask having the Digimouse shape since, after the last two steps, the actual CT image has the same shape.

In these three steps, we have used the following Elastix registration parameters:

- All calculations are made with floating-point precision;
- Multi-resolution registration at 5 levels with down-sampling factors of 32, 16, 8, 4 and 2, each with 1st order B-spline image smoothing and with 4096, 4096, 2048, 2048 and 1024 iterations, respectively;
- The adopted metric is the normalized correlation coefficient, since it performs slightly better (than for example Mutual Information) when registering images from the same modality.
- The image sampler was composed of 2500 random points that were actualized on each iteration.
- The optimizer used is the adaptive stochastic gradient descent that chooses the step size of the optimizer.
- The final interpolator is calculated using a 3rd order B-spline function.

As explained earlier, after each registration step, *elastix* writes the transformation parameters. When this is done, we use these parameters as input for *transformix* software to transform actual mouse PET and segmented images.

E. Characterization of image registration

Segmented images of the fixed and moving images are required to evaluate the performance of the image registration algorithm. In our case, the fixed image is the Digimouse CT image which already has a corresponding atlas consisting of 21 body regions. We were unable to reproduce an equivalent segmentation and as such we have instead segmented seven

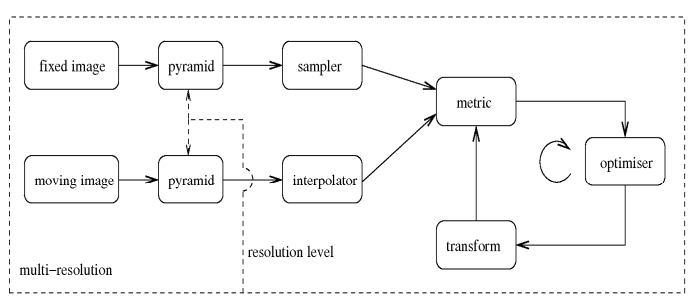

The basic registration components.

Fig. 4. Schema of the modular construction of the Elastix image registration software (from the Elastix Users manual by Stefan Klein and Marius Staring).

regions all over the mouse body that were reproducible and were also present in the Digimouse atlas: brain, lungs, heart, kidneys, bladder, skeleton and rest of the body. To quantify the influence of our segmentation on the final result, we have segmented the same regions on the Digimouse CT image. This segmentation was performed using the ITK Snap software [21] which allows semi-automated image segmentation.

Various methods were proposed to evaluate the accuracy of image registration and segmentation methods. These can be classified into 3 different categories [22]: volume and surface overlap, volume similarity and distance or discrepancy measures. We have selected the two most popular metrics which seem to be the most significant to characterize the accuracy of image registration:

a) *Dice Coefficient (D_{coeff}) or Mean Overlap*: This is a volume overlap metric which quantifies the intersection between source and target labels divided by their mean volume:

$$D_{coeff} = 2\frac{\sum_r |S_r \cap T_r|}{\sum_r (|S_r| + |T_r|)} \quad (1)$$

Dice coefficient [23] is a special case of Kappa statistical coefficient [24] which can be interpreted as follows:

- Poor agreement = Less than 0.20
- Fair agreement = 0.20 to 0.40
- Moderate agreement = 0.40 to 0.60
- Good agreement = 0.60 to 0.80
- Excellent agreement = 0.80 to 1.00

b) *Hausdorff Distance (HD)*: This is the most frequently used discrepancy measure that represents the maximum distance we would need to move the boundaries of the source region to completely cover the target region:

$$HD_{S\to T} = \max_{s\in S}\left\{\min_{t\in T}\{d(s,t)\}\right\} \quad (2)$$

Where s and t are points of the Source (S) and target (T) regions respectively, and $d(s,t)$ is the distance between them. $HD_{S\to T}$ is oriented or asymmetric (a property of maximum function while minimum function is symmetric), and most of the time it is not equal to $HD_{T\to S}$,. For this reason the generalized Hausdorff distance (HD) is defined as:

$$HD = \max\left\{\max_{s\in S}\left\{\min_{t\in T}\{d(s,t)\}\right\}, \max_{t\in T}\left\{\min_{s\in S}\{d(s,t)\}\right\}\right\} \quad (3)$$
$$= \max\{HD_{S\to T}, HD_{T\to S}\}$$

F. Automated analysis of PET data

The overall activity was normalized by each mouse maximum activity to obtain so-called normalized mean activity (NMA).

In the absence of ground truth, we used the normalized mean activity values from the pre-registered PET images for the 7 segmented regions as reference values. Automated PET analysis was performed by measuring the normalized mean activity in regions of the original Digimouse segmentation and compared it with reference values.

Table I. Summary of registration results for the 8 laboratory mice and 17 simulated mice with original Digimouse segmentation.

	Mouse	Dice Coefficient [0,1]		Hausdorff Distace (mm)	
		Mean	SD	Mean	SD
Real	PINlab	.4567	.2843	6.41	3.46
	m23124	.4302	.2746	7.55	5.13
	m23212	.4886	.2708	7.02	5.15
	m25629	.5943	.2083	5.24	3.83
	m27308	.5274	.2468	5.10	2.92
	Mouse 1	.3075	.2755	6.83	2.17
	Mouse 2	.4729	.2506	5.62	2.88
	Mouse 3	.3316	.3056	6.88	1.74
Simulated	Moby1	.4453	.2566	5.96	2.68
	Moby2	.4431	.2608	6.04	2.70
	Moby3	.4446	.2569	5.93	2.65
	Moby4	.4552	.2582	5.97	2.68
	Moby5	.4444	.2588	5.95	2.70
	Moby6	.4507	.2627	5.93	2.75
	Moby7	.4530	.2650	6.00	2.66
	Moby8	.4281	.2676	6.25	2.77
	Moby9	.4554	.2590	5.91	2.68
	Moby10	.4587	.2626	5.93	2.82
	Moby11	.4489	.2609	6.11	2.68
	Moby12	.4503	.2602	5.98	2.76
	Moby13	.4509	.2622	5.98	2.72
	Moby14	.4471	.2617	5.95	2.66
	Moby15	.4613	.2610	5.99	2.74
	Moby16	.4470	.2631	6.11	2.71
	Moby17	.4080	.2627	6.49	2.48

III. Results and Discussion

A. Image registration algorithm

As stated earlier, image registration between the actual mouse and the Digimouse CT images was performed without the use of fiducial markers. Figure 5 show examples of best and worst registration results using this procedure, respectively. The only minor data pre-processing step used was the preparation of both datasets to have similar fields-of-view (FOVs) (Fig. 5; third row).

1) Laboratory mice

The Dice Coefficient (D_{coeff}) and the Hausdorff Distance (HD) results for all segmented regions of the actual mice are summarized in Table I. The values are calculated between the transformed segmentation and the original Digimouse segmentation.

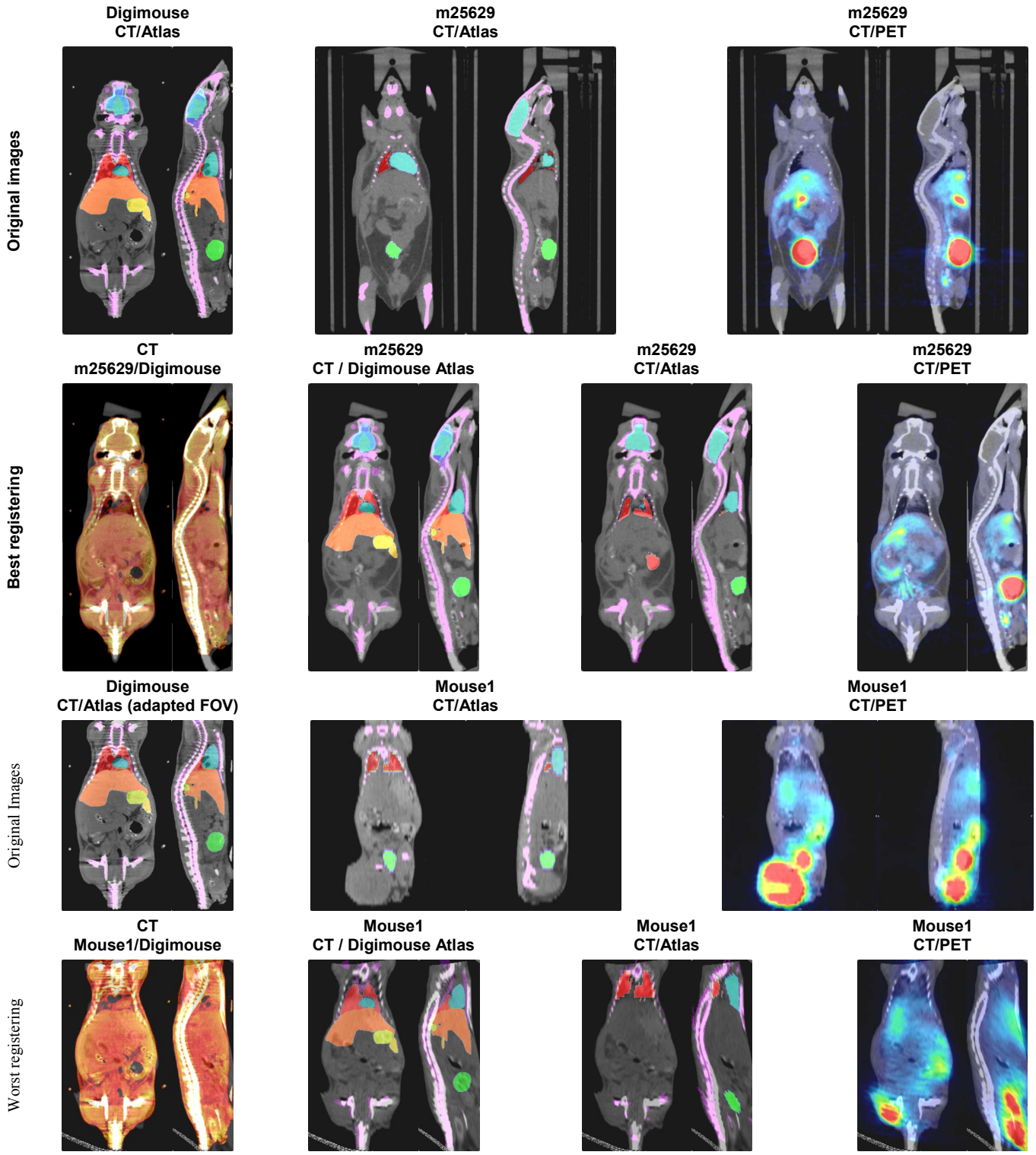

Fig. 5. Original images of the Digimouse and the mouse m25629 (first row) which resulted in the best registeration results (second row) together with the original images of the adapted FOV Digimouse and the mouse Mouse1 (third row), which resulted in the worst registration (last row).

The same figures of merit were also calculated using our Digimouse segmentation. The difference between the results was calculated and tested through a t-test of correlated samples that have shown that there is a significant mean improvement on D_{coeff} of 0.0475 (p<0.0001), but a non-significant improvement on the *HD* (mean improvement of 0.17 mm; p=0.143).

Dice coefficient show that only 2 mice registrations present only fair overall agreement with Digimouse model (means of 0.3075 and 0.3316) while the rest are registered with moderate agreement (0.4302 to 0.5943) (Table I).

On table II, we show "by organ" registration accuracy results where one can see that in all cases body shape (remaining organs and skin) is registered with good agreement

Table II. Characterization of image registration using the Digimouse segmentation for 7 regions of the 8 laboratory mice and for 12 regions for the 17 simulated mice.

Region	Type of mice	Dice Coefficient [0,1]					Hausdorff Distance (mm)					NMA relative difference (%)				
		Min.	Med.	Max.	Mean	SD	Min.	Med.	Max.	Mean	SD	Min.	Med.	Max.	Mean	SD
Brain	Simulated	.8359	**.8479**	.8654	**.8482**	.0082	1.44	**1.70**	1.91	**1.70**	0.13	-4.00	**-1.35**	1.69	**-1.01**	1.46
	Real	.8083	**.8310**	.8548	**.8296**	.0181	1.94	**2.49**	3.62	**2.57**	0.64	-17.38	**-1.49**	2.43	**-3.75**	8.08
Heart	Simulated	.4642	**.5348**	.5699	**.5364**	.0244	3.11	**3.23**	5.16	**3.34**	0.47	-5.87	**-2.60**	-0.29	**-2.77**	1.47
	Real	.2001	**.5011**	.6828	**.4847**	.1461	2.25	**3.83**	5.16	**3.75**	0.85	-176.8	**1.80**	35.24	**-19.26**	67.12
Lungs	Simulated	.5010	**.5519**	.5736	**.5480**	.0175	3.61	**3.76**	3.90	**3.76**	0.08	-0.13	**1.38**	3.53	**1.37**	1.00
	Real	.0703	**.4197**	.6509	**.3566**	.2128	3.01	**4.64**	7.52	**4.97**	1.72	-124.0	**5.05**	28.05	**-16.43**	52.38
Kidneys	Simulated	.4263	**.4509**	.4985	**.4550**	.0188	3.63	**3.98**	4.69	**4.01**	0.30	32.15	**34.97**	36.35	**34.54**	1.25
	Real	.2306	**.4004**	.4812	**.3867**	.0860	3.26	**4.08**	6.32	**4.48**	1.05	-43.49	**15.35**	48.08	**8.10**	28.20
Bladder	Simulated	.0000	**.0000**	.0000	**.0000**	.0000	9.04	**9.39**	10.07	**9.42**	0.25	93.95	**94.27**	94.75	**94.35**	0.22
	Real	.0000	**.1302**	.6385	**.1851**	.2301	2.26	**6.22**	11.95	**6.80**	2.99	0.27	**78.37**	97.36	**64.57**	36.83
Skeleton	Simulated	.2974	**.3117**	.3258	**.3126**	.0077	9.01	**9.22**	9.48	**9.23**	0.13	-5.79	**-3.87**	-0.76	**-3.70**	1.37
	Real	.1944	**.2727**	.3779	**.2796**	.0638	5.82	**10.36**	15.45	**10.76**	3.20	-7.46	**-1.61**	27.16	**3.37**	12.88
Remaining organs&Skin	Simulated	.7583	**.7668**	.7739	**.7662**	.0042	9.30	**9.47**	9.59	**9.45**	0.07	2.91	**4.73**	7.77	**4.83**	1.28
	Real	.7630	**.8130**	.8390	**.8079**	.0268	4.94	**9.15**	14.04	**9.56**	3.16	-1023	**-43.42**	6.84	**-250.27**	367.46
Liver	Simulated	.6056	**.6591**	.6828	**.6566**	.0173	5.20	**6.08**	6.51	**5.97**	0.29	4.27	**6.01**	8.95	**6.12**	1.16
Pancreas	Simulated	.0063	**.0395**	.0509	**.0357**	.0121	8.24	**8.49**	8.72	**8.49**	0.12	-149.1	**-129.8**	-105.2	**-129.8**	11.18
Spleen	Simulated	.2192	**.4019**	.4343	**.3874**	.0560	4.20	**4.73**	6.43	**4.84**	0.55	2.47	**8.16**	12.67	**8.17**	2.38
Stomach	Simulated	.4222	**.5298**	.5516	**.5241**	.0311	4.42	**4.62**	6.84	**4.82**	0.60	-11.55	**-5.25**	-1.33	**-5.37**	2.06
Testis	Simulated	.2699	**.2897**	.3022	**.2890**	.0096	7.00	**7.26**	7.46	**7.30**	0.12	-238.3	**-217.0**	-168.8	**-208.5**	19.55

while brain is registered with excellent agreement. Heart registration has moderate agreement while the remaining regions are registered only with fair agreement.

The interpretation of *HD* results is a little more difficult to decode because of the dependency of this value on organ size. Nevertheless, one can see that organ mismatch is generally below 5 mm, with three exceptions: skeleton and "remaining organs and skin" where *HD* is above 11 mm because of their large size, and the bladder where it is ~ 6 mm because of the high mobility of this organ. Here again brain registration achieved the best results with mismatches in the order of 2.5 mm.

2) Simulated mice

As discussed in paragraph II.A, since over 50% of the laboratory mice included in this study are present with transplanted tumor xenografts resulting in large morphological deformations, we clearly expect most uniform results with simulated mice which only reflect standard size and activity variations of normal mice. This can be seen on table I where simulated mice produce Dice coefficients between 0.4446 and 0.4613, with only one mouse showing a lower value (Moby 17: 0.4080).

This is also noticeable on Table II, where variations on Dice coefficients for different regions are lower, while the mean values of simulated mice are not systematically higher. Hausdorff distance results behave similarly to the Dice coefficients.

The same comparison can be seen on figure 6 where we show Box and Whisker plots for all regions.

B. PET automated analysis

1) Laboratory mice

PET normalized mean activity concentration was calculated using the original and our Digimouse segmentation. The improvement obtained using our segmentation (1.2%) was not considered statistically significant (p=0.214).

One can also see the relative error on the automated quantification of the normalized mean activity in Fig. 6 (bottom row) and table II. Caution is needed for interpretation of "remaining organs and skin" regions for two reasons. First, the segmentation is different between actual and simulated mice samples, and second, for mice images obtained on the LabPET™ scanner (GE Healthcare), an artificial increase of activity concentration was already noticed only by the transformation of original images (from 153% to 941%) while in other regions these transformations keep the original activity concentration within -1.9%. This artificial increase of activity is due to the presence of a large lesion on the right leg of mice (third row on figure 5).

2) Simulated mice

The results of simulated mice studies demonstrate that the mean and median values are close to experimental mice values, but with lower standard deviations (table II). Problematic organs (e.g. bladder, pancreas) present very large

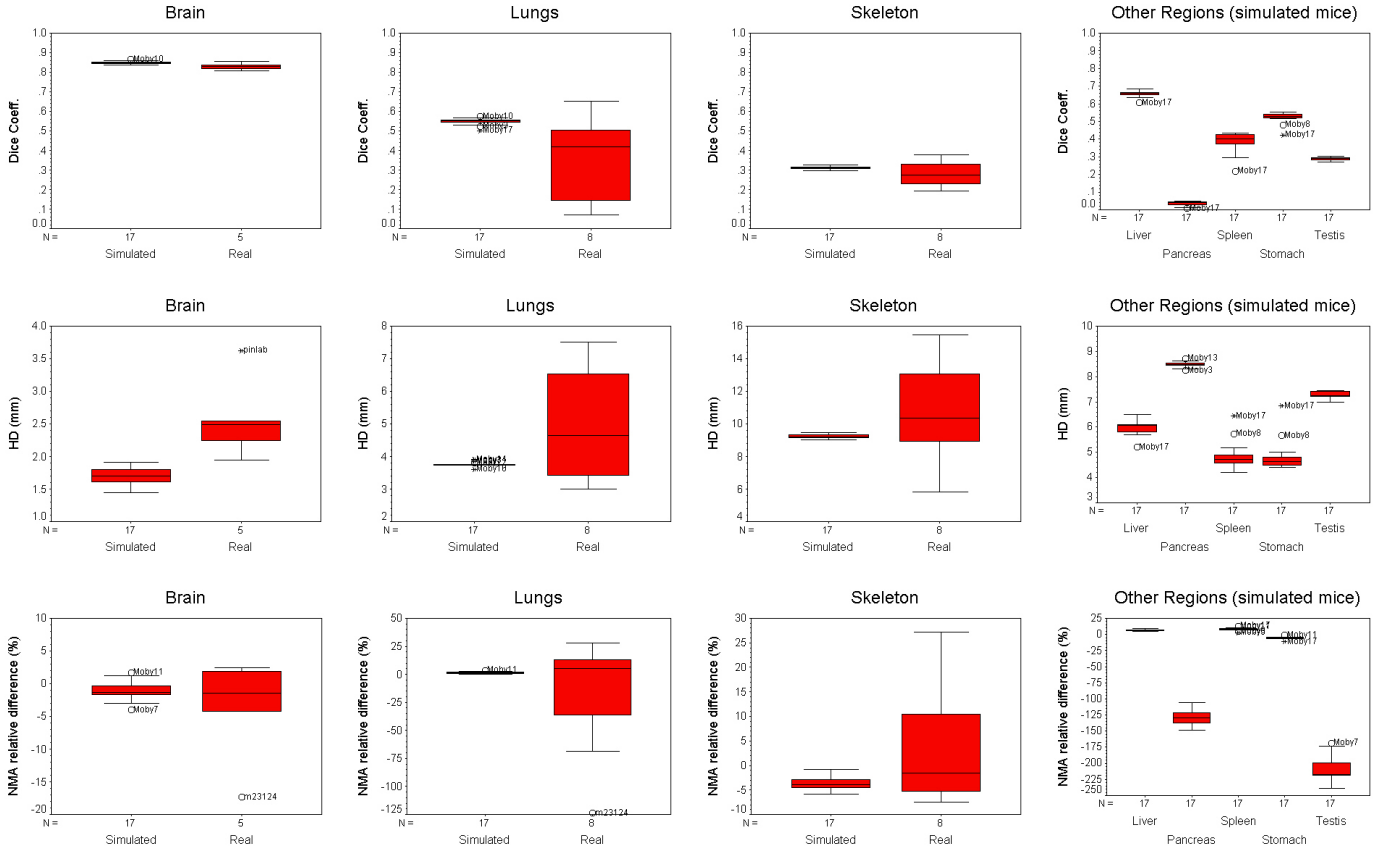

Fig. 6. Box and Whisker plots of 8 real and 17 simulated mice for the 7 and 12 segmented regions respectively. Top: Dice Coefficient results. Middle: Hausdorff Distance results. Bottom: Normalized Mean Activity (NMA) relative difference for automatic assessment results.

deviations from original values. This was, however, expected from image registration assessment results. On contrary, one can observe that the normalized mean activity resulting from the automated quantification technique is stable for most other regions since the mismatch is below 10%. The brain shows again the lowest mean error (-1.01%).

Table III. Correlation coefficients (R^2) resulting from linear regression analysis between actual (harvested) and measured PET activity concentration for simulated mice.

Automated Our method		**Semi-automated** Kesner et al.[4]		
			Software	**Manual**
Moby1	0.954	Mouse 1	0.943	0.083
Moby2	0.961	Mouse 2	0.957	0.973
Moby3	0.950	Mouse 3	0.947	0.956
Moby4	0.952	Mouse 4	0.893	0.825
Moby5	0.965	Mouse 5	0.908	0.560
Moby6	0.800	Mouse 6	0.999	0.276
Moby7	0.797	Mouse 7	0.934	0.915
Moby8	0.879	Mouse 8	0.483	0.424
Moby9	0.764	Mouse 9	0.996	0.992
Moby10	0.961			
Moby11	0.767			
Moby12	0.832			
Moby13	0.842			
Moby14	0.749			
Moby15	0.890			
Moby16	0.796			
Moby17	0.749			
Mean	**0.859**	**Mean**	**0.896**	**0.667**

Kesner *et al.* [4] compared measured SUVs obtained from manual delineation to software-based segmentation obtained using a semi-automated registration technique. Linear regressions were performed between these estimates and those resulting from what they called the *harvested SUV* obtained from dissected organs. In our case, we were not able to perform similar experiments and as such we have considered the *harvested* normalized mean activity as the actual input activity introduced in the voxel-based phantom.

Correlation coefficient (R^2) of these linear regressions for the 9 mice simulated by Kesner and for our 17 mice are shown on table III as a mean of 6 segmented regions (heart, brain, lungs, liver, spleen and kidneys). Similar results between the two techniques were obtained. The same analysis was also performed for each individual segmented region (Table IV), again with comparable results.

The disadvantage of the proposed technique in comparison with Kesner's method is that PET/CT images are required by our method while Kesner's uses only PET images. Nevertheless, the advantage of our method is that it is fully automated; the only user interaction needed is to select similar fields of view.

Table IV. Correlation coefficients (R^2) resulting from linear regression analysis between actual (harvested) and measured PET activity concentration for different ROIs.

	Automated Our method	**Semi-automated** Kesner et al.[4]	
		Software	**Manual**
Heart	0.526	0.579	0.358
Brain	0.309	0.331	0.237
Lung	0.677	0.799	0.303
Liver	0.489	0.589	0.192
Spleen	0.229	0.038	0.193
Kidneys	0.584	0.636	0.513
Stomach	0.432	na	na
Skin	0.490	na	na
Skeleton	0.299	na	na
Pancreas	0.441	na	na
Testis	0.033	na	na

IV. Conclusion

We proposed a method allowing automated quantification of preclinical PET studies. To this effect, PET/CT images of the mouse study adaptation of the actual mouse and atlas fields-of-view are required.

The automated quantification is achieved by 3D image registration between CT images of the mouse and the Digimouse atlas. The transformations achieving this were afterwards applied to PET images to align actual PET/CT to the Digimouse *image space*. The Digimouse segmentation is used to define the regions of interest to be evaluated.

This method has proved to perform as good as other techniques where user action is needed (e.g. Kesner *et al.* [4]). Normalized mean activity measurement was preserved between reference and automated measures in most of the considered regions with relative errors below 10%. The only regions presenting with higher relative errors are regions corresponding to small mobile organs such as the testicles, bladder, kidneys and pancreas. This was, however, expected from image registration assessment results.

Acknowledgements

This work was supported by the Swiss National Science Foundation under grant SNSF 3152A0-102143.

References

[1] S. S. Gambhir, "Molecular imaging of cancer with positron emission tomography.," *Nat Rev Cancer,* vol. 2, pp. 683-693, 2002.

[2] C. Casteels, P. Vermaelen, J. Nuyts, A. Van Der Linden, V. Baekelandt, L. Mortelmans, G. Bormans, and K. Van Laere, "Construction and evaluation of multitracer small-animal PET probabilistic atlases for voxel-based functional mapping of the rat brain.," *J Nucl Med,* vol. 47, pp. 1858-1866, 2006.

[3] D. J. Rubins, W. P. Melega, G. Lacan, B. Way, A. Plenevaux, A. Luxen, and S. R. Cherry, "Development and evaluation of an automated atlas-based image analysis method for microPET studies of the rat brain.," *Neuroimage,* vol. 20, pp. 2100-2118, 2003.

[4] A. L. Kesner, M. Dahlbom, S. C. Huang, W. A. Hsueh, S. P. B, J. Czernin, M. Kreissl, H. M. Wu, and D. H. Silverman, "Semiautomated analysis of small-animal PET data.," *J Nucl Med,* vol. 47, pp. 1181-1186, 2006.

[5] W. P. Segars, B. M. Tsui, E. C. Frey, G. A. Johnson, and S. S. Berr, "Development of a 4-D digital mouse phantom for molecular imaging research.," *Mol Imaging Biol,* vol. 6, pp. 149-159, 2004.

[6] B. Dogdas, D. Stout, A. F. Chatziioannou, and R. M. Leahy, "Digimouse: a 3D whole body mouse atlas from CT and cryosection data.," *Phys Med Biol,* vol. 52, pp. 577-587, 2007.

[7] R. Taschereau, P. L. Chow, and A. F. Chatziioannou, "Monte Carlo simulations of dose from microCT imaging procedures in a realistic mouse phantom.," *Med Phys,* vol. 33, pp. 216-224, 2006.

[8] M. G. Stabin, T. E. Peterson, G. E. Holburn, and M. A. Emmons, "Voxel-based mouse and rat models for internal dose calculations.," *J Nucl Med,* vol. 47, pp. 655-659, 2006.

[9] L. Wu, G. Zhang, Q. Luo, and Q. Liu, "An image-based rat model for Monte Carlo organ dose calculations.," *Med Phys,* vol. 35, pp. 3759-3764, 2008.

[10] H. Zaidi and X. G. Xu, "Computational anthropomorphic models of the human anatomy: The path to realistic Monte Carlo modeling in medical imaging.," *Annu Rev Biomed Eng,* vol. 9, pp. 471-500, 2007.

[11] J. B. Maintz and M. A. Viergever, "A survey of medical image registration.," *Med Image Anal,* vol. 2, pp. 1-36, 1998.

[12] J. P. Pluim, J. B. Maintz, and M. A. Viergever, "Mutual-information-based registration of medical images: a survey.," *IEEE Trans Med Imaging,* vol. 22, pp. 986-1004, 2003.

[13] P. Slomka and R. Baum, "Multimodality image registration with software: state-of-the-art.," *Eur J Nucl Med Mol Imaging,* vol. 36, pp. 44-55, 2009.

[14] P. B. Zanzonico, "Broad-spectrum multi-modality image registration: from PET, CT, and MRI to autoradiography, microscopy, and beyond.," *Conf Proc IEEE Eng Med Biol Soc,* vol. 1, pp. 1584-1588, 2006.

[15] S. Klein, M. Staring, K. Murphy, M. A. Viergever, and J. P. Pluim, "elastix: a toolbox for intensity-based medical image registration," *IEEE Trans Med Imaging,* vol. 29, p. 9, 2010.

[16] R. Prasad, O. Ratib, and H. Zaidi, "Performance evaluation of the FLEX Triumph™ X-PET scanner using the NEMA NU-04 standards.," *J Nucl Med,* vol. 51, pp. 1608-1615, 2010.

[17] W. P. Segars, M. Mahesh, T. J. Beck, E. C. Frey, and B. M. W. Tsui, "Realistic CT simulation using the 4D XCAT phantom.," *Med Phys,* vol. 35, pp. 3800-3808, 2008.

[18] L. A. Feldkamp, L. C. Davis, and J. W. Kress, "Practical cone-beam algorithm," *J. Opt. Soc. Am. A,* vol. 1, pp. 612-619, 1984.

[19] K. Thielemans, S. Mustafovic, and C. Tsoumpas, "STIR: Software for Tomographic Image Reconstruction Release 2," in *Nuclear Science Symposium Conference Record, 2006. IEEE*, 2006, pp. 2174-2176.

[20] M. Jacobson, R. Levkovitz, A. Ben-Tal, K. Thielemans, T. Spinks, D. Belluzzo, E. Pagani, V. Bettinardi, M. C. Gilardi, A. Zverovich, and G. Mitra, "Enhanced 3D PET OSEM reconstruction using inter-update Metz filtering.," *Phys Med Biol,* vol. 45, pp. 2417-2439, 2000.

[21] P. A. Yushkevich, J. Piven, H. C. Hazlett, R. G. Smith, S. Ho, J. C. Gee, and G. Gerig, "User-guided 3D active contour segmentation of anatomical structures: significantly improved efficiency and reliability," *Neuroimage,* vol. 31, pp. 1116-28, 2006.

[22] A. Klein, J. Andersson, B. A. Ardekani, J. Ashburner, B. Avants, M. C. Chiang, G. E. Christensen, D. L. Collins, J. Gee, P. Hellier, J. H. Song, M. Jenkinson, C. Lepage, D. Rueckert, P. Thompson, T. Vercauteren, R. P. Woods, J. J. Mann, and R. V. Parsey, "Evaluation of 14 nonlinear deformation algorithms applied to human brain MRI registration," *Neuroimage,* vol. 46, pp. 786-802, 2009.

[23] L. R. Dice, "Measures of the Amount of Ecologic Association Between Species," *Ecology,* vol. 26, pp. 297-302, 1945.

[24] A. P. Zijdenbos, B. M. Dawant, R. A. Margolin, and A. C. Palmer, "Morphometric analysis of white matter lesions in MR images: method and validation," *IEEE Trans Med Imaging,* vol. 13, pp. 716-24, 1994.